



Formation of hierarchical Ni₃S₂ nanohorn arrays driven by *in-situ* generation of VS₄ nanocrystals for boosting alkaline water splitting

Dan Yang^a, Liyun Cao^a, Liangliang Feng^{a,b,*}, Jianfeng Huang^a, Koji Kajiyoshi^b, Yongqiang Feng^a, Qianqian Liu^a, Wenbin Li^a, Li Feng^a, Guojuan Hai^a

^a School of Materials Science & Engineering, Shaanxi Key Laboratory of Green Preparation and Functionalization for Inorganic Materials, Shaanxi University of Science and Technology, Xi'an Shaanxi 710021, PR China

^b Research Laboratory of Hydrothermal Chemistry, Faculty of Science and Technology, Kochi University, Kochi, 780-8520, Japan

ARTICLE INFO

Keywords:

Ni₃S₂
VS₄
Nanohorn arrays
Water splitting

ABSTRACT

The synergistic achievement of geometric optimization and surface/interfacial modulation of electrocatalysts for booting the overall efficiency of water splitting is highly desirable yet challenging. Herein, a novel hierarchical Ni₃S₂/VS₄ nanohorn array grown on nickel foam (NS-horn/NF) is prepared by a self-driven synthesis strategy. We demonstrate that *in-situ* generation of VS₄ in the NS-horn/NF not only triggers the formation of such unique hierarchical architecture, but favors the graft of enriched active bridging S₂²⁻ on the strong coupling interface between Ni₃S₂ and VS₄, and thus the enhanced HER kinetics. More importantly, the abundant active nickel oxides for the OER available form on the interface benefiting from the surface reconstruction of NS-horn/NF due to the partial leaching of vanadium (IV) of VS₄, which promotes the adsorption of OH⁻ and leads to the fast OER rate-determining step in alkaline media. When employed to assemble an alkaline electrolyzer as both anode and cathode, NS-horn/NF electrode only needs a small voltage of 1.57 V to yield 10 mA cm⁻² and retains this activity for at least 70 h. Our findings put forward fresh insights into the rational design of highly efficient bifunctional electrocatalysts toward water splitting for next-generation energy conversion and storage devices.

1. Introduction

Cost-effective electrocatalytic water splitting holds great promise for the sustainable production of clean hydrogen fuel and powerfully advances the implementation of “Hydrogen Economy” [1–3]. The overall efficiency of water electrolysis depends on the simultaneous reaction kinetics of both half reactions involving the hydrogen evolution reaction (HER) and oxygen evolution reaction (OER) [4]. While the kinetically sluggish OER, particularly, greatly impedes the highly efficiency of water splitting for hydrogen production due to its intrinsic four consecutive proton and electron transfer steps [5–7]. Additionally, Pt-based materials and Ir or Ru oxides can efficiently catalyze the HER and OER, respectively, but the development and wide application are extremely restricted due to their single function, high price and low earth-abundance [8,9]. There is a dire need to develop the integrating Janus electrocatalysts with low-cost and highly active activity for overall water splitting [10].

Up to now, great advances have been achieved to develop high-performance bifunctional electrocatalysts based on cheap and earth-

abundant transition metals for water splitting, such as metal oxides [11–13], chalcogenides [14–16], carbides [17–19] and phosphides [20–22]. Among of them, Ni₃S₂ is a typical representative of transition metal chalcogenides and exists in nature in the mineral heazlewoodite, which has been intensively investigated as a highly promising electrocatalyst for overall water splitting due to its unique configuration, metallic conductivity and excellent chemical stability [14,23,24]. Previously substantial efforts have been devoted to find synthetic tweaks enhancing the overall efficiency of water splitting over Ni₃S₂-based materials, most of which usually make great progress on the HER activity while the unsatisfied improvement of OER because of the ignorance of boosting the adsorption ability of the catalyst toward OER intermediates, especially for OH⁻ species in alkaline media [25–27]. Recently, VS₄, an emerging potential vanadium (IV) polysulfide containing bridging S₂²⁻ moieties, has been intensely explored as metal-ion storage materials owing to its unique characteristics of one-dimensional chain-like crystal structure with a big interchain distance, relatively high electronic conductivity and high sulfur content [28–30]. Rationally incorporating VS₄ into the Ni₃S₂ material has been taken into

* Corresponding author at: School of Materials Science & Engineering, Shaanxi Key Laboratory of Green Preparation and Functionalization for Inorganic Materials, Shaanxi University of Science and Technology, Xi'an Shaanxi 710021, PR China.

E-mail address: fengll@sust.edu.cn (L. Feng).

<https://doi.org/10.1016/j.apcatb.2019.117911>

Received 16 March 2019; Received in revised form 31 May 2019; Accepted 29 June 2019

Available online 01 July 2019

0926-3373/ © 2019 Elsevier B.V. All rights reserved.

consideration to improve its overall water dissociation kinetics. On the one hand, vanadium (IV) in VS_4 with great affinity to oxygen atoms could be accessibly leached once exposed to a strong alkaline media under oxidizing potentials [31], leading to the available formation of active nickel oxides due to the surface reconstruction effect and thus favors the OH^- absorption for OER in alkaline media [32–34]. On the other hand, the unsaturated bridging S_2^{2-} grafted on the surface of $\text{Ni}_3\text{S}_2/\text{VS}_4$ hybrids functions as not only active HER sites, but also an electron acceptor by virtue of the structure feature -S-S- units, both of which contribute to the HER and OER simultaneously [35–37]. To the best of our knowledge, until now, impressive electrocatalysts involving VS_4 have not yet been exploited for overall water splitting. Besides, since the catalytic reactions usually take place on the surface of the catalysts, construction of 3D hierarchical structure has been demonstrated to be effective method to increase abundant accessible active sites to the electrolyte and facilitate the mass and electron transportation, eventually leading to the improved electrocatalytic performance [38–41]. Therefore, hierarchical Ni_3S_2 nanoarchitectures integrating with VS_4 are considerably challengeable and highly expectative for efficient water electrolysis.

Herein, we report, for the first time, the elaborate synthesis of a 3D hierarchical $\text{Ni}_3\text{S}_2/\text{VS}_4$ nanohorn arrays grown on nickel foam driven by *in situ* generation of VS_4 nanocrystals in a facile solvothermal synthetic system, and the as-obtained electrode is denoted as NS-horn/NF. Benefiting from numerous catalytically active sites, abundant active bridging S_2^{2-} and the great affinity of OH^- radicals on the coupling interface between Ni_3S_2 and VS_4 , the resulting NS-horn/NF exhibited the higher catalytic performance for HER and OER compared to the NS-hill/NF counterpart. When applied as both the anode and cathode to assemble an alkaline electrolyzer, NS-horn/NF displays a low applied potential of 1.57 V to motivate the water-splitting at 10 mA cm^{-2} and remains the catalytic stability for at least 70 h. In addition, this constructional strategy of hierarchical nanoarchitecture in our work can be extended to the preparation of other functional materials.

2. Experimental work

2.1. Materials

All chemicals were of reagent grade and used without further purifications. Sodium orthovanadate ($\text{Na}_3\text{VO}_4 \cdot 12\text{H}_2\text{O}$) was purchased from Aladdin. Thioacetamide (TAA, CH_3CSNH_2), ethanol and potassium hydroxide (KOH) were purchased from Sinopharm Chemical Reagent Co., Ltd. (China). Platinum on activated carbon (20 wt% Pt/C, Pt on an activated carbon support) was purchased from Sigma-Aldrich. IrO_2 catalyst was purchased from Alfa Aesar. Highly purified water ($> 18 \text{ M}\Omega \text{ cm}$ resistivity) was provided by a PALL PURELAB Plus system. Ni foam (thickness: 1.5 mm, bulk density: 0.23 g/cm^3) was purchased from Suzhou Jiashide foam metal Co., Ltd. Ni foam (abbreviated as NF) was cleaned ultrasonically with acetone and 3 M HCl solution for 10 min in each, then washed subsequently with water and ethanol for several times to ensure the clean surface.

2.2. Synthesis of NS-horn/NF

The hierarchical $\text{Ni}_3\text{S}_2/\text{VS}_4$ nanohorn arrays grown on Ni foam were synthesized via a facile solvothermal method. In a typical procedure, 150 mg of sodium orthovanadate ($\text{Na}_3\text{VO}_4 \cdot 12\text{H}_2\text{O}$) and 150 mg of thioacetamide (TAA, CH_3CSNH_2) were mixed in 20 mL of absolute ethanol accompanied by magnetic stirring for 30 min. The as-prepared suspension then was transferred into a 50 mL Teflon-lined autoclave containing a piece of treated NF ($1 \text{ cm} \times 5 \text{ cm}$). The autoclave was sealed and heated up to 180°C for 20 h. Afterward the system was allowed to cool down to room temperature. The as-prepared material was washed with distilled water and ethanol for several times, and dried in a vacuum at room temperature, denoted as NS-horn/NF.

2.3. Synthesis of NS-hill/NF

The synthetic procedure of NS-hill/NF is similar to that of NS-horn/NF. The only difference between them lies in removing the sodium orthovanadate in the reaction system.

2.4. Materials characterization

X-ray diffraction (XRD) patterns were recorded using a D8 Advance X-ray diffractometer with $\text{Cu K}\alpha$ radiation ($\lambda = 0.15406 \text{ nm}$). Field emission scanning electron microscope (FESEM, Hitachi, S-4800), transmission electron microscopy (TEM, Tecnai G2 F20S-TWIN) and atomic force microscopy (AFM 5100, Agilent) were used to characterize the morphologies and the nanostructures. The elemental compositions and chemical states were analyzed by an AXIS SUPRA X-ray photoelectron spectrometer (XPS) using monochromatic $\text{Al K}\alpha$ radiation as the X-ray source. The Raman spectra was obtained using a Renishaw-invia Microscopic confocal laser Raman spectrometer with 532 nm as the excitation laser. ICP-AES was performed using a THEM 6300 ICP spectrometer. N_2 adsorption/desorption isotherms were measured with Micromeritics ASAP2460 sorption analyzer.

2.5. Electrochemical tests

All electrochemical measurements were performed with a three-electrode system using a CHI Instrument (Model 660E), in which NS-horn/NF was used directly as the working electrode. Prior to the experiments, the NS-horn/NF electrode was sealed on all edges with a modified acrylate adhesive except for the working surface area (0.12 cm^2). A graphite rod was used as the counter electrode and Hg/HgO as the reference electrode. All the potentials were converted to values with the reference to a reversible hydrogen electrode (RHE) according to the following equation: $E(\text{RHE}) = E(\text{Hg/HgO}) + 0.098 + 0.0591 \times \text{pH}$. A scanning rate of 1 mV/s was used for linear sweep voltammetry measurements. The Electrochemical impedance spectroscopy (EIS) was recorded at a biasing potential of 0.6 V for OER and -1.25 V for HER with the frequency range from 100 kHz to 0.01 Hz in 1.0 M KOH solution. To compare the relative electrochemical active area, cyclic voltammetry measurements were carried out on NS-horn/NF and NS-hill/NF at different scan rates (10 mV s^{-1} , 20 mV s^{-1} , 40 mV s^{-1} , 80 mV s^{-1} etc.) in 0–0.1 V vs. RHE range for OER and then the potential of 0.05 V vs RHE was chosen to estimate the double-layer capacitance (C_{dl}), which are linearly proportional to the effective electrochemical active area. For the powder samples (20 wt% Pt/C, IrO_2 and VS_4), 28.32 mg of the powder and 100 μL of isopropanol were mixed. Then 10 μL of the above solution and 2 μL of 0.3% Nafion solution were drop-casted on Ni foam with a mass loading of $\sim 23.6 \text{ mg cm}^{-2}$.

3. Results and discussion

3.1. Structure characterization

As schematically illustrated in Fig. 1, 3D hierarchical $\text{Ni}_3\text{S}_2/\text{VS}_4$ nanohorn array *in situ* grown on nickel foam (hereafter denoted as NS-horn/NF) were synthesized via a facile one-step solvothermal reaction by a mixed solution consisting of $\text{Na}_3\text{VO}_4 \cdot 12\text{H}_2\text{O}$, thioacetamide (TAA) and ethanol, as well as a piece of Ni foam (NF, $1 \text{ cm} \times 5 \text{ cm}$) as scaffold at 180°C for 20 h. Firstly, the crystal structure and composition of NS-horn materials scraped from NF were analyzed by the X-ray diffraction (XRD) pattern. As shown in Fig. 2A, the diffraction peaks in XRD pattern of NS-horn/NF at 21.9° , 31.2° , 37.9° , 44.6° , 49.8° and 55.3° match well with (101), (110), (003), (202), (113) and (122) plane of hexagonal Ni_3S_2 phase (PDF # 44-1418). In addition, two obvious diffraction peaks located at 15.7° and 17° can be assigned to (110) and (020) plane of monoclinic VS_4 (PDF # 72-1294), respectively, and the

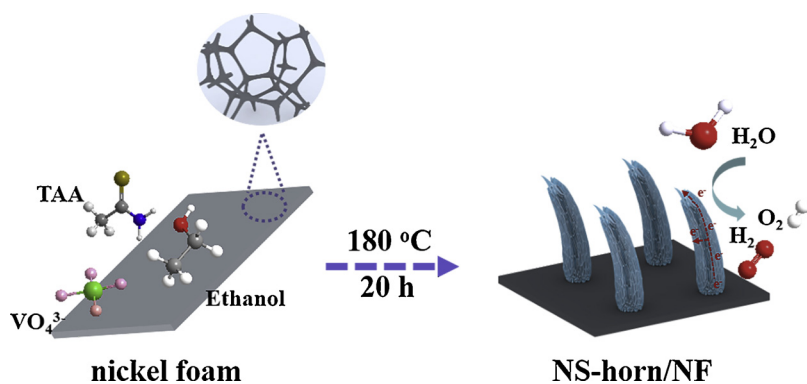


Fig. 1. A schematic illustration of the synthesis process of NS-horn/NF.

formed VS_4 material presents the preferable growth orientation along vertical direction of (020) plane, indicating the successful preparation of the hybrid material of Ni_3S_2 and VS_4 on NF substrate.

In order to investigate the morphology and microstructure of NS-horn/NF, scanning electron microscopy (SEM) and transmission electron microscopy (TEM) images were conducted by us. The SEM image of pure NF displays a smooth and clean surface after removing the oxide layer with the acid treatment (Fig. S1), whereas those of NS-horn/NF in Fig. 2B and insert show that Ni foam skeletons are uniformly covered by dense nanohorn arrays. And, the surface of the nanohorns is comprised of vertically spatial nanosheets, as further revealed in the SEM image with a high magnification (Fig. 2C). The AFM image and height file of Fig. S2 further confirmed the nanosheets' thickness of 4–6 nm, indicating its ultrathin feature. Moreover, the high-resolution TEM

(HRTEM) image of NS-horn/NF gives the extremely clear lattice fringes with interplanar distance of 0.287 nm and 0.237 nm corresponding to the (110) plane and the (003) facet of Ni_3S_2 , respectively, and with the interlayer spacing of 0.52 nm assigned to (020) plane of VS_4 (Fig. 2D and S3). And, the associated selected-area electron diffraction (SAED) pattern of Fig. 2D inset shows the discrete and bright diffraction spots, indicating the high crystallinity of the Ni_3S_2 and VS_4 , which is well coincided with the XRD results. Fig. 2E–H exhibits the TEM image of a single $\text{Ni}_3\text{S}_2/\text{VS}_4$ horn extracted by ultrasonically treatment of the NS-horn/NF sample and the corresponding elemental mapping images. It is revealed that the Ni, V and S elements are distributed over the whole horn-architecture, with a higher Ni and S concentration in the center of the horn-architecture; while V homogeneously exists in the entire horn-architecture, suggesting that such hierarchical architecture is

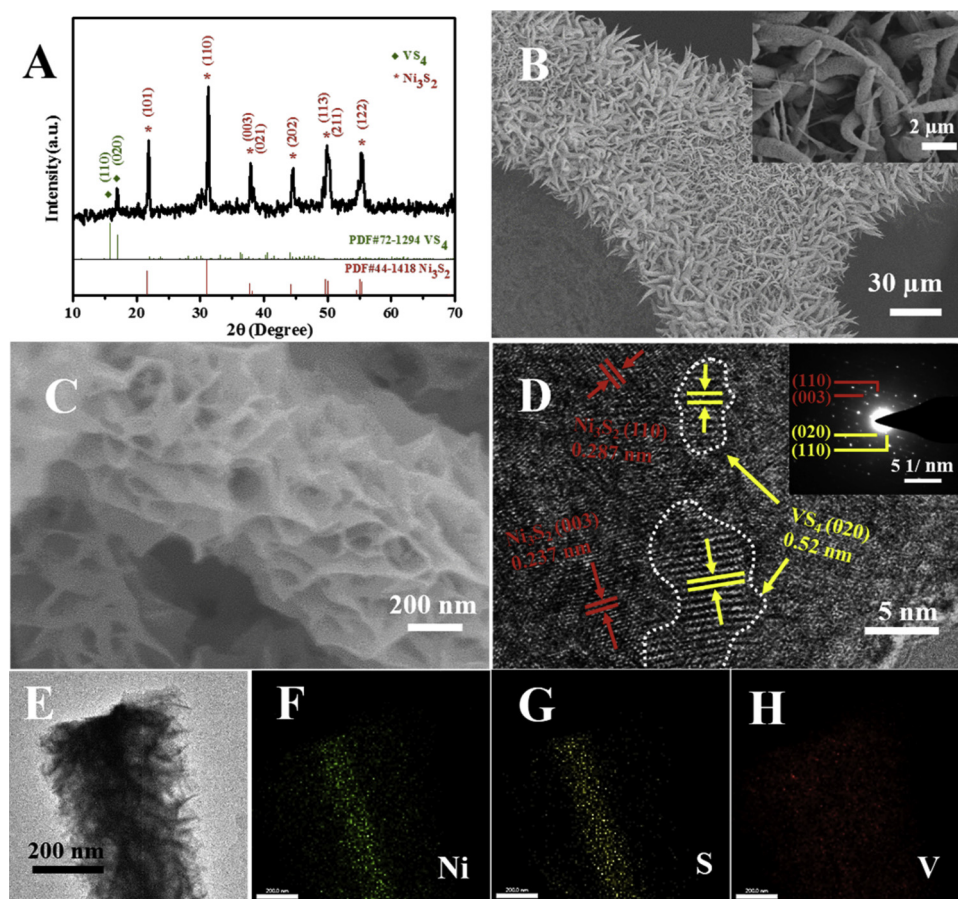


Fig. 2. (A) XRD pattern, (B–C) SEM images, (D) HRTEM image of NS-horn/NF, with SAED pattern shown in the inset, (E) TEM image and (F–H) the corresponding elemental mapping images of NS-horn/NF.

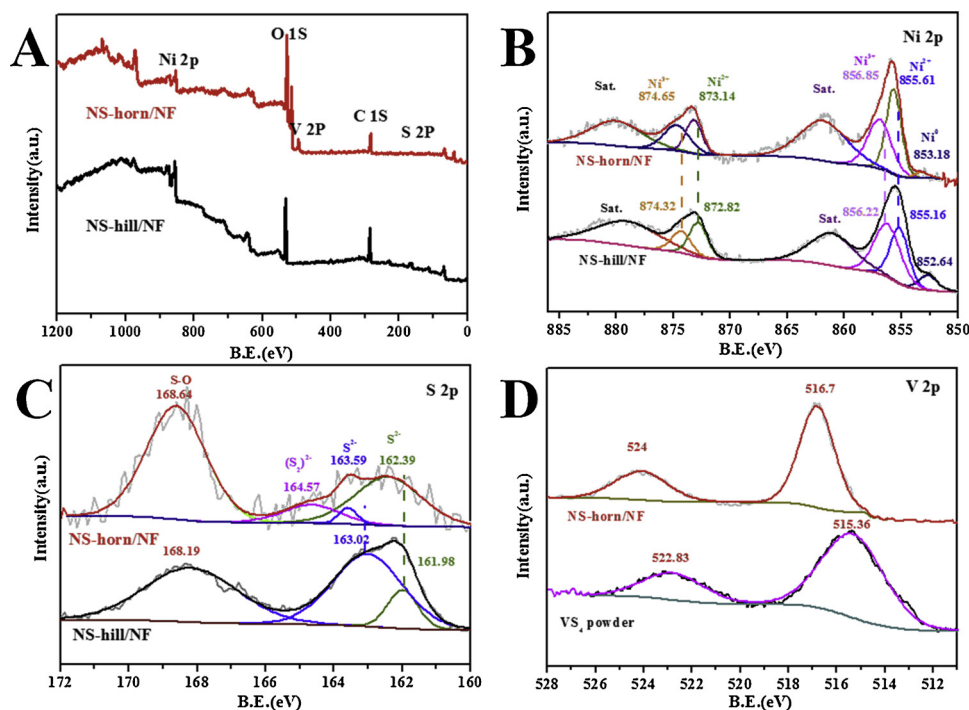


Fig. 3. High-resolution XPS spectra: (A) Survey, (B) Ni 2p and (C) S 2p of NS-horn/NF and NS-hill/NF, (D) V2p of NS-horn/NF and pure VS₄.

assembled by 2D ultrathin nanosheets and 1D nanorods and *in-situ* generation of VS₄ nanocrystals drives the formation of the hierarchical Ni₃S₂/VS₄ nanohorn arrays grown the NF. Furthermore, inductively coupled plasma atomic emission spectrometry (ICP-AES) determines a molar ratio of V: Ni is about 1: 2.5 and the mass loadings is $\sim 23.6 \text{ mg cm}^{-2}$ in the NS-horn/NF material.

X-ray photoelectron spectroscopy (XPS) measurement was performed to further investigate the surface chemical and electronic states of NS-horn/NF. In the survey XPS spectrum of NS-horn/NF, elemental peaks for Ni, O, V, C and S are observed (Fig. 3A). Spectrum peaks with the binding energy of 855.61 eV in Ni 2p_{3/2} and 873.14 eV in Ni 2p_{1/2} are in agreement with the characteristic of Ni²⁺, and the peaks with binding energy of 856.85 eV in Ni 2p_{3/2} and 874.65 eV in Ni 2p_{1/2} are typically ascribed to Ni³⁺, accompanying by their respective satellite peaks except for the peak of Ni⁰ [42,43]. Obviously, the Ni 2p_{1/2} peak of NS-horn/NF shows a positive shift of $\sim 0.32 \text{ eV}$ compared to that of NS-hill/NF (Fig. 3B). The high-resolution S 2p spectrum of NS-horn/NF (Fig. 3C) shows that the S 2p_{3/2} and S 2p_{1/2} peaks are observed at 162.39 eV and 163.59 eV, respectively, which are attributed to S²⁻ in Ni₃S₂, and the S 2p_{3/2} peak of NS-horn/NF show a positive shift of $\sim 0.41 \text{ eV}$ with respect to that of NS-hill/NF, while the peak at 164.57 eV is ascribed to the emerging bridging disulfide (S₂)²⁻ of VS₄ in NS-horn/NF [44,45]. The quantitative analysis of the S 2p high-resolution XPS fitting spectrum reveals that the (S₂)²⁻/(S_{total}) atomic ratio in the NS-horn/NF is about 10.3: 100, and (S₂)²⁻:(V + Ni + S_{total}) atomic ratio in the NS-horn/NF is about 7: 100, indicating that the density of the active bridging (S₂)²⁻ sites on the surface of NS-horn/NF is about 7%. In the V 2p region, the peaks located at 516.7 eV and 524 eV are attributed to V 2p_{3/2} and V 2p_{1/2}, which are characteristic of V⁴⁺, confirming the formation of VS₄ phase in the NS-horn/NF (Fig. 3D) [28,29,46]. Moreover, the V 2p peaks of NS-horn/NF show the similar positive shifts with both Ni 2p and S 2p peaks compared to that of VS₄ powder, which could result in the accumulation of negative charges on the bridging (S₂)²⁻ species with more dangling bonds, and therefore favoring the adsorption of H⁺ intermediates [36,37,47]. Meanwhile, the above results also indicate the existence of strong electronic interactions between VS₄ and Ni₃S₂ in NS-horn/NF, which is significantly conducive to the charge transfer and reaction dynamics of

electrocatalysis process [34].

3.2. Growth mechanism

In order to investigate the growth mechanism of NS-horn/NF, several key experimental parameters for such material are firstly discussed below. First of all, it was found that the addition and amount of sodium orthovanadate played major roles in the formation of NS-horn/NF. When sodium orthovanadate was not used in the reaction, a rough hill-like Ni₃S₂ thin film rather than 3D hierarchical nanohorn arrays was formed over the NF (Fig. S4). When the amount of sodium orthovanadate was decreased to the half in the reaction, nanohorns composed of larger and thicker nanosheets were obtained, but the density of which relatively decreased, resulting in the decreased catalytic active sites (Fig. S5). While the amount of sodium orthovanadate was doubled, the similar 3D hierarchical nanohorn arrays emerged with a much denser nanosheets arrangement (Fig. S6), which is not conducive to the mass transport of the water splitting intermediates. As a result, NS-horn/NF has a better catalytic activity than these two samples (Fig. S7). Secondly, ethanol functioning as the solvent is highly indispensable to the generation of the 3D hierarchical Ni₃S₂/VS₄ nanohorn arrays. When deionized water was used, in lieu of ethanol, in the synthesis, the Ni₃S₂ nanowires containing amorphous VS₄ were formed on NF (Fig. S8D), proved by the facts that the V⁴⁺ and (S₂)²⁻ existing in XPS spectra (Fig. S8A, B) and no VS₄ phase detected in XRD pattern (Fig. S8C), which has a lower catalytic activity than NS-horn/NF (LSV curves see Fig. S8E). At last, when a small amount of nickel powder was used, in place of NF, a Ni₃S₂/VS₄ hybrid comprising of nanorods and nanoparticles was formed (Fig. S9). If nickel salt substituted for NF in the synthesis system, NiS₂/V₃Ni(SO₄)₄(H₂O)₂₄ nanoparticles rather than Ni₃S₂/VS₄ hybrids were obtained (Fig. S10). As a whole, sodium orthovanadate, ethanol as well as NF are great of significance for the microstructural and compositional formation of NS-horn/NF. Additionally, time-dependent control experiments were conducted in the following. When the reaction time was 5 h, 1D Ni₃S₂/VS₄ nanorods appeared and covered uniformly on the surface of NF (Fig. S11A, Fig. 4A and B), which had the limited contact area with electrolyte compared to NS-horn/NF. With reaction time increasing to 10 h, the nanosheets gradually grown

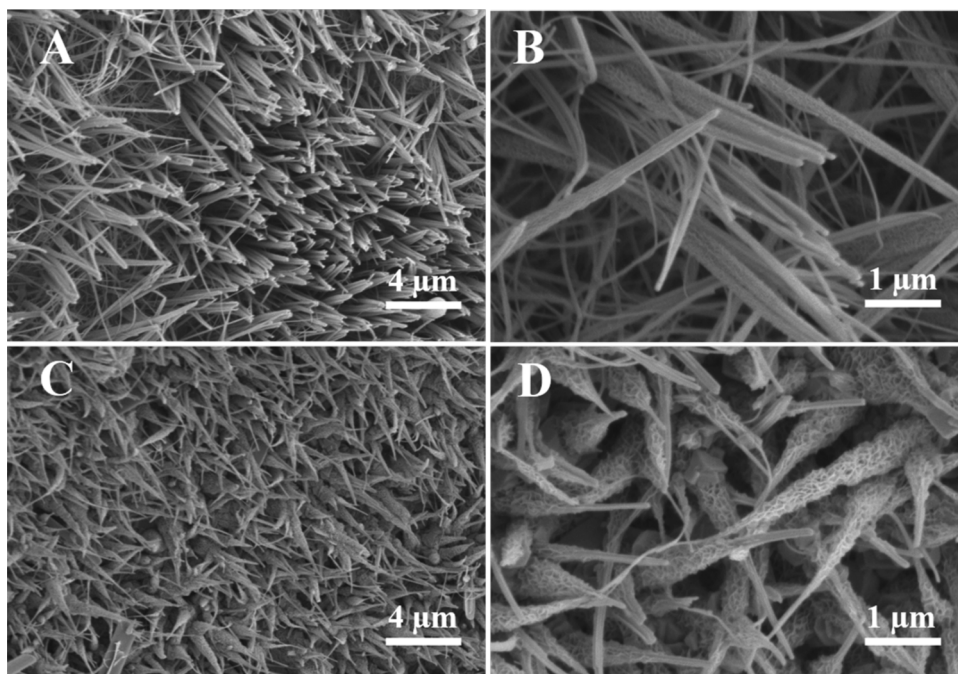


Fig. 4. SEM images of the samples prepared with different reaction times while other conditions were kept unchanged: 5 h (A and B), and 10 h (C and D).

on the surface of the nanorods and resulted in the occurrence of hierarchical nanohorn-like structure with a high contact area with electrolyte (Fig. S11B, Fig. 4C and D). As the reaction time prolonged to 20 h, the density of nanosheets on the nanorods obviously increased and eventually leading to the formation of 3D hierarchical $\text{Ni}_3\text{S}_2/\text{VS}_4$ nanohorn arrays on NF (Fig. 2B). As expected, as shown in Fig. S11D, NS-horn/NF exhibited the best catalytic activity among the three samples mainly due to the well-defined 3D hierarchical structure for the increased catalytic sites and the large contact area with electrolyte for fast mass transportation during electrocatalysis. The results also indicate that regulating the reaction time does not give rise to the phase change but the controllable microstructure for optimizing the material's catalytic performance (Fig. S11C).

Considering all the results presented above, the growth mechanism of 3D hierarchical nanohorn arrays on NF can be proposed as follows. Owing to the insolubility of Na_3VO_4 in ethanol solvent, a small amount of nickel ions generated on the surface of NF suffering from the etching of TAA where preferentially reacting with S^{2-} to form Ni_3S_2 crystal nucleus containing a tiny amount of Na_3VO_4 . Simultaneously, with the aid of the ethanol as reductant for reducing V^{5+} to V^{4+} at high temperature [31], the formed Ni_3S_2 is speculated to be a template for the nucleation and growth of VS_4 nanocrystals, this result is based on the fact that no VS_4 phase is obtained without adding the nickel sources (eg. NF or nickel powders) in the synthetic system (Fig. S12) and the relevant previous reports [28,48]. Subsequently, *in situ* generation of VS_4 nanocrystals with a one-dimensional chain structure induced the spiral upward growth of Ni_3S_2 , which could be triggered by the interchain dispersion forces of VS_4 , leading to the formation of nanorods in a shorter reaction time (Fig. 4A and B). As the reaction proceeding, the nanorod structure gradually evolved into the hierarchical nanohorn structure due to its uneven growth resulting from the inhomogeneous diffusion of Ni^{2+} from NF's surface toward the solution. For the electrochemical contribution of VS_4 , pure VS_4 material was obtained according to the previous report (Fig. S13A and S13B) [49] and then OER and HER activity of pure VS_4 on GCE or NF were investigated, respectively. The LSV curves show that pure VS_4 has the intrinsic electrochemical inactivity for the HER and OER (Fig. S13C, D and S14A, B). The above results demonstrate that the in-situ generation of VS_4 in the synthesis system mainly contributed to the formation and surface

modulation of 3D hierarchical Ni_3S_2 nanohorn arrays structure.

3.3. Electrochemical activity of NS-horn/NF

We evaluated the electrocatalytic activity of NS-horn/NF for OER in alkaline electrolyte using a standard three-electrode system without *iR* compensation. For comparison, NS-hill/NF, IrO_2 /NF and NF were also studied under the same condition. The linear sweep voltammetry (LSV) curves of these samples have demonstrated that the NS-horn/NF only needs an overpotential of 317 mV to yield a large current density of 50 mA cm^{-2} , with a nearly four-fold enhancement in catalytic activity compared to NS-hill/NF at the identical overpotential, which is significantly lower than IrO_2 /NF (370 mV) and NF (500 mV) (Fig. 5A). The reaction kinetics of NS-horn/NF were further examined by Tafel plot. By fitting polarization curves to the Tafel equation ($\eta = b \times \log j + a$, where j is the current density, and b is the Tafel slope), we got the Tafel plots of the samples. In the potential region of 1.3–1.4 V, the Tafel slope of the NS-horn/NF (43 mV/dec) is much smaller than that of NS-hill/NF (120 mV/dec), indicating the fast surface oxidation of Ni_3S_2 to active nickel oxides, which is mainly contributed to the high affinity of V atoms in VS_4 to oxygenated species and high surface area delivered by the NS-horn/NF arrays. In the region of 1.55–1.65 V, NS-horn/NF shows a larger Tafel slope (200 mV/dec) compared to NS-hill/NF (157 mV/dec), which could be resulted from the formation of a large overlapping peaks from the oxidation peak of nickel, suggesting that the formation of $\text{O} = \text{O}$ is the OER rate-limiting step (Fig. 5B) [42,50]. Besides, a multi-step chronoamperometric curve for NS-horn/NF is obtained to evaluate the electrocatalytic OER stability (Fig. 5C). The overpotential starts at 50 mV and ends at 500 mV with an increment of 50 mV every 500 s. The result shows that the current density remains quite stable at each overpotential in the entire test range, indicating the highly durability during OER electrocatalysis. This can be further validated by the *I-t* and LSV curves (Fig. 5D, Fig. S15 and S16A), obviously, only an insignificant current variation is observed even for over 50 h. More importantly, NS-horn/NF retains a high faraday efficiency after 50 h-OER electrolysis (~94%) compared to the initial faraday efficiency (Fig. S16B, C).

To get more insights into the electrocatalytic properties, the electrochemically active surface area (ECSA) and electrochemical

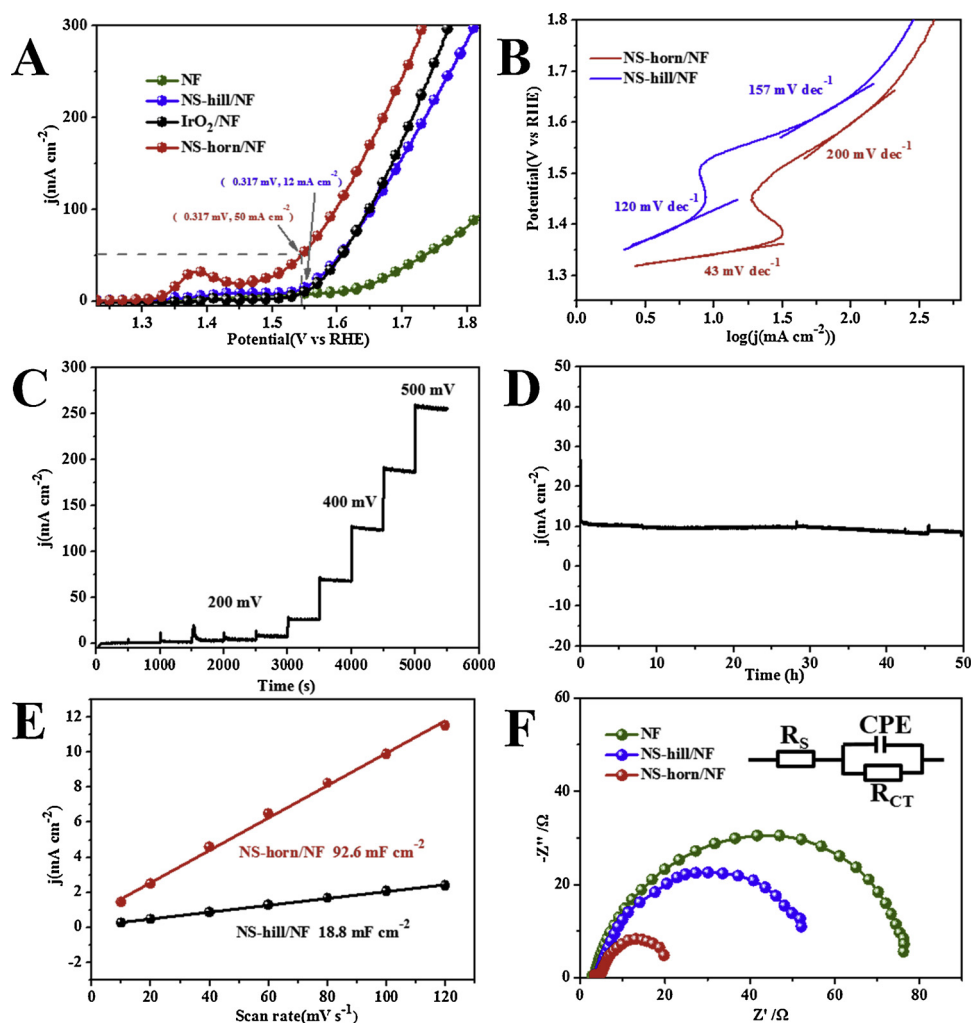


Fig. 5. (A) OER polarization curves of NF, NS-hill/NF, NS-horn/NF and IrO₂/NF without *iR* correction and (B) Tafel plots of NS-hill/NF and NS-horn/NF. (C) Multi-step chronoamperometric curves of OER over NS-horn/NF in 1.0 M KOH solution. (D) Chronopotentiometry curve of NS-horn/NF in 1.0 M KOH at a constant current density of 10 mA cm⁻². (E) electrochemical double-layer capacitance (*C_{dl}*) of NS-horn/NF and NS-hill/NF. (F) Electrochemical impedance spectroscopy (EIS) Nyquist plots of NF, NS-hill/NF and NS-horn/NF.

impedance spectroscopy (EIS) were carried out. The cyclic voltammograms (CV) of NS-horn/NF and NS-hill/NF were firstly recorded in a nonfaradic region from 0 to 0.1 V (Fig. S17A and S17B) and then the potential of 0.05 V vs RHE was chosen for the calculation of *C_{dl}*. The electrochemical double-layer capacitance (*C_{dl}*) is linearly proportional to the electrochemical active surface area (ECSA). The fitting results in Fig. 5E show that the ECSA of NS-horn/NF is 4.9 times higher than that of the NS-hill/NF, demonstrating the more enriched active sites in NS-horn/NF for the OER, which can be further confirmed by the comparative BET surface areas from N₂-adsorption measurements (Fig. S18). Besides, EIS curves were measured and the fitting results can be acquired through the equivalent circuit (Fig. 5F inset). The values of charge-transfer resistance (*R_{ct}*) of NS-horn/NF, NS-hill/NF and NF are found to be 15.44 Ω, 46.4 Ω and 67.73 Ω, respectively (Table S1). Comparison of the results suggests that the electron transfer process in OER over NS-horn/NF is much faster than those over NS-hill/NF and NF, indicating it possess outstanding electron conductivity and therefore fast reaction kinetics during electrocatalytic OER.

In order to examine the origin of the excellent OER catalytic performance, the SEM, XRD, TEM, Raman and XPS data of NS-horn/NF after 50 h OER electrolysis were characterized here. The XRD pattern of Fig. S19 firstly reveals that Ni₃S₂ and VS₄ phases still retain in this material. From the SEM image of Fig. S20A, it is found that the morphology of NS-horn/NF is subject to some destruction due to the partial

leaching of vanadium of the hybrids (Fig. S22), while the nanorod structure remains in the material (Fig. S20B). And, the surface chemical states of NS-horn/NF after the catalytic stability test have been further evaluated. The Ni 2p_{1/2} peaks of NS-horn/NF show negative shifts of ~ 0.6 eV after OER stability test with respect to the initial ones, and the ratio of Ni³⁺/Ni²⁺ greatly increases from 1.01 to 2.03 (Fig. 6A). This result could be associated to the formation of more active NiOOH species on the surface of NS-horn/NF, which is supported by the Raman spectrum and HRTEM images of NS-horn/NF after 50 h OER electrolysis (Fig. 6C-F) and can be accelerated by the surface reconstruction of NS-horn/NF resulting from the partial leaching of VS₄ in a strong alkaline media (Fig. S21 and S22), and thus leading to the faster OER kinetics [51,52]. Besides, the adsorption of OH⁻ play a vital role and is the kinetic rate-determining step for the OER in alkaline media [34,51]. From the O1 s high-resolution XPS spectrum, we can see that the O1 s peak could be fitted into three peaks O₁, O₂ and O₃, which are attributed to the metal-oxygen bond, the surface hydroxyls, and the adsorbed oxygen, respectively [53,54] (Fig. 6B). Apparently, the larger area of O₂ after OER test implies that more adsorbed OH⁻ radicals are generated on the surface of NS-horn/NF, attributed to the existence of active nickel oxides with the strong absorption towards OH⁻ radicals [51,52].

Besides operating well as an OER electrocatalyst in alkaline media, the NS-horn/NF was also found to be a remarkably excellent electrocatalyst for the HER in the identical condition. As illustrated in LSV

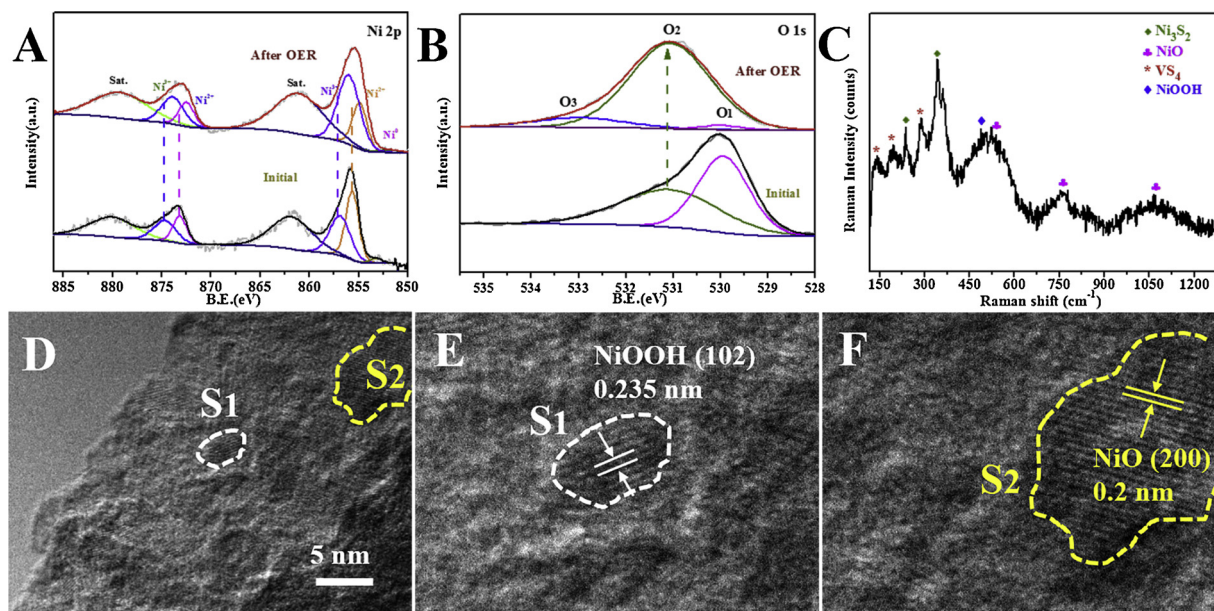


Fig. 6. (A) Ni 2p and (B) O 1s XPS spectra before and after OER chronoamperometry test, (C) Raman spectrum, (D, E, F) HRTEM images of NS-horn/NF after OER chronoamperometry test.

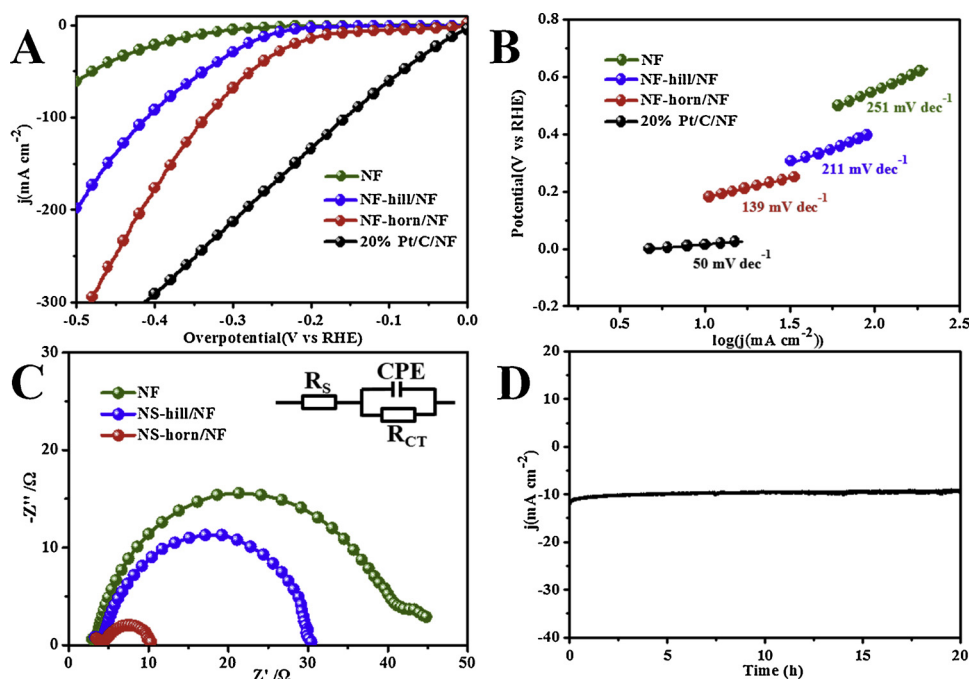


Fig. 7. (A) HER polarization curves and (B) Tafel plots of NF, NS-hill/NF, NS-horn/NF, 20%Pt/C/NF, (C) Electrochemical impedance spectroscopy (EIS) Nyquist plots of NF, NS-hill/NF and NS-horn/NF. (D) Chronopotentiometry curve of NS-horn/NF at a constant current density of 10 mA cm⁻².

curves of Fig. 7A, the 20% Pt/C/NF undoubtedly displays the best catalytic HER activity among these samples. Compared to other samples, the NS-horn/NF can offer 10 mA cm⁻² at a very low overpotential of 177 mV, much lower than those of NS-hill/NF (253 mV) and NF (345 mV). Besides, the Tafel plots of the samples are obtained in Fig. 7B. The plots fitted value for NS-horn/NF is 139 mV dec⁻¹, which is larger than that of 20% Pt/C/NF but smaller than NS-hill/NF (211 mV dec⁻¹), and NF (251 mV dec⁻¹), suggesting the faster kinetics of the Volmer step-determined HER [33,55]. This also can be affirmed by the faster charge transfer of NS-horn/NF indicated in EIS results (Fig. 7C). Given that the Volmer pathway ($\text{H}_2\text{O} + \text{e}^- + \text{M} \rightarrow \text{M-H}_{\text{ad}}^* + \text{OH}^-$) is the rate-determining step of NS-horn/NF for the HER in alkaline media,

its faster HER kinetics compared to NS-hill/NF can be ascribed to the following aspects. (i) The 3D hierarchical nanohorn arrays can expose more catalytic active sites for the water adsorption. (ii) The coupling interface with a strong hydrophilicity enhances the ability of water adsorption (Fig.S23). (iii) The strong OH⁻ adsorption ability is very conducive to cleaving the HO-H bonds for forming H_{ad}^{*} on the surface of NS-horn/NF (Fig.S24) [34,56]. (iv) The abundant bridging (S₂)²⁻ on the surface of NS-horn/NF provides more highly active sites for the HER [36,37]. Moreover, the NS-horn/NF can give an excellent stability for at least 20 h in alkaline operating condition (Fig. 7D), accompanied by the well-maintained composition and microstructure (Fig.S25 and S26).

Inspired by our finding that NS-horn/NF exhibited outstanding

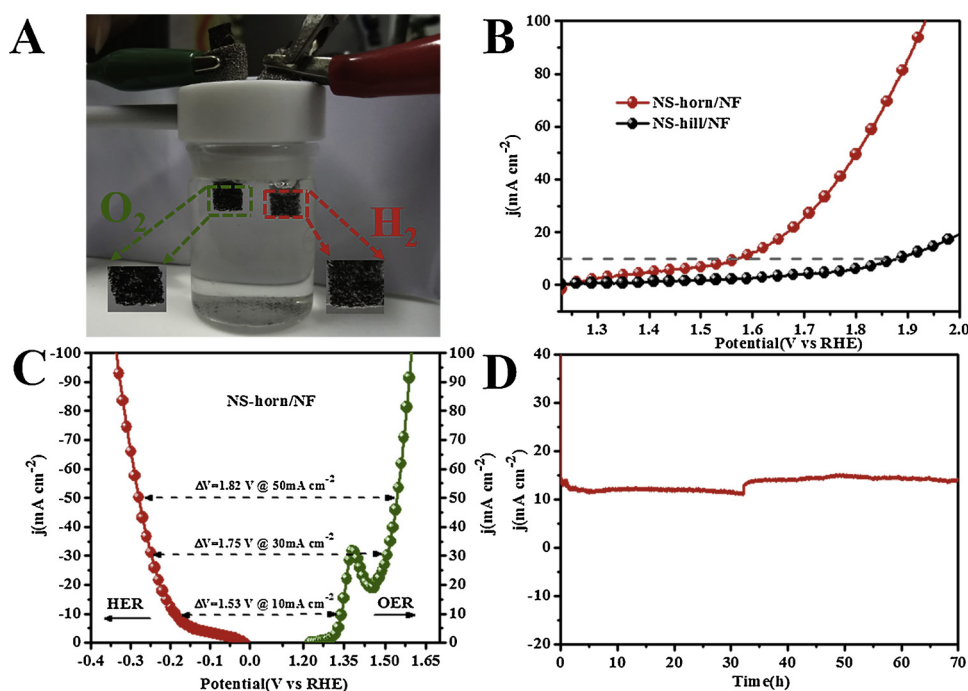


Fig. 8. (A) Optical image of NS-horn/NF electrode and overall water-splitting device. (B) Polarization curve of NS-horn/NF and NS-hill/NF for overall water splitting in 1.0 M KOH. (C) Steady-state polarization curves of NS-horn/NF for HER and OER. (D) Chronopotentiometry curve of NS-horn/NF for water splitting at 15 mA cm⁻² in a 1 M KOH solution.

bifunctional property as electrocatalyst for both OER and HER, an alkaline electrolyzer was assembled by the NS-horn/NF as both anode and cathode simultaneously (Fig. 8A). The electrolyzer affords a current density of 10 mA cm⁻² at an applied voltage of only 1.57 V (Fig. 8B), which is smaller than the electrolyzer comprising NS-hill/NF (1.88 V). Also, the applied voltages of NS-horn/NF for overall water splitting is consistent with the voltage difference between HER and OER at the same current density (10 mA cm⁻²) with negligible differences coming from the changes of chemical environment (Fig. 8C). What's more, the I-t curve in Fig. 8D shows that NS-horn/NF couple can maintain the current density of 15 mA cm⁻² for over 70 h toward overall water splitting, indicating the pronounced catalytic durability. The above results reveal that NS-horn/NF can be functioned as a promising and superior electrocatalyst for overall water splitting (see Table S2-4).

4. Conclusions

In summary, we report the rational design and synthesis of a novel 3D hierarchical Ni₃S₂/VS₄ nanohorn array grown on nickel foam (NS-horn/NF). The growth mechanism of NS-horn/NF is systematically investigated and experimental results reveal that *in-situ* generation of VS₄ in the NS-horn/NF not only contributes to the formation of such unique hierarchical architecture, but favors the graft of enriched active bridging S₂²⁻ on the strong coupling interface between Ni₃S₂ and VS₄, both of which are very conducive to promoting the HER kinetics. Moreover, benefiting from the affinity to oxygen atoms for vanadium (IV) of VS₄, the abundant active nickel oxides for the OER readily form on the reconstructional surface with the partial leaching of VS₄, which enhances the adsorption of OH⁻ and leads to the fast OER rate-determining step in alkaline media. Therefore, the NS-horn/NF catalyst exhibits remarkable electrocatalytic activity for HER, OER and overall water splitting. Our findings not only provide an effective strategy for the rational design of hierarchical functional electrocatalysts, but also offers in-depth understanding of the surface modification and evolution of catalysts and broadens our horizons to create more efficient electrocatalytic materials for practical application.

Conflict of interest

None.

Acknowledgements

This work was supported by National Natural Science Foundation of China (No.21701107, 51672165, 21603243), Natural Science Foundation of Shaanxi Province (2019JQ-018), Doctoral Scientific Research Startup Foundation of Shaanxi University of Science and Technology (2016QNBT-07), Natural Science Foundation of Shaanxi Provincial Department of Education (17JK0093), Beijing National Laboratory for Molecular Sciences (BNLMS201805), Platform construction Fund for Imported talent of Shaanxi University of Science and Technology (134080038) and National Key R&D Program of China (2017YFB0308300).

Appendix A. Supplementary data

Supplementary material related to this article can be found, in the online version, at doi:<https://doi.org/10.1016/j.apcatb.2019.117911>.

References

- [1] S. Chu, A. Majumdar, Opportunities and challenges for a sustainable energy future, *Nature* 488 (2012) 294–303, <https://doi.org/10.1038/nature11475>.
- [2] F.M. Sapountzi, J.M. Gracia, C.J. Weststrate, H.O.A. Fredriksson, J.W. Niemantsverdriet, Electrocatalysts for the generation of hydrogen, oxygen and synthesis gas, *Prog. Energy Combust. Sci.* 36 (2010) 307–326, [https://doi.org/10.1016/0360-1285\(84\)90120-5](https://doi.org/10.1016/0360-1285(84)90120-5).
- [3] X. Zou, Y. Zhang, Noble metal-free hydrogen evolution catalysts for water splitting, *Chem. Soc. Rev.* 44 (2015) 5148–5180, <https://doi.org/10.1039/c4cs00448e>.
- [4] Z. Kai, D. Zhang, Recent progress in alkaline water electrolysis for hydrogen production and applications, *Prog. Energy Combust. Sci.* 36 (2010) 307–326, <https://doi.org/10.1016/j.pecs.2009.11.002>.
- [5] B. You, Y. Sun, Innovative strategies for electrocatalytic water splitting, *Acc. Chem. Res.* 51 (2018) 1571–1580, <https://doi.org/10.1021/acs.accounts.8b00002>.
- [6] F. Lyu, Q. Wang, S.M. Choi, Y. Yin, Noble-metal-free electrocatalysts for oxygen evolution, *Small* 15 (2019) 1804201, <https://doi.org/10.1002/smll.201804201>.
- [7] W. Zhu, Z. Yue, W. Zhang, N. Hu, Z. Luo, M. Ren, Z. Xu, Z. Wei, Y. Suo, J. Wang, Wet-chemistry topotactic synthesis of bimetallic iron-nickel sulfide nanoarrays: an advanced and versatile catalyst for energy efficient overall water and urea electrolysis, *J. Mater. Chem. A* 6 (2018) 4346–4353, <https://doi.org/10.1039/C7TA10584C>.

- [8] T. Reier, M. Oezaslan, P. Strasser, Electrocatalytic oxygen evolution reaction (OER) on Ru, Ir, and Pt catalysts: a comparative study of nanoparticles and bulk materials, *ACS Catal.* 2 (2012) 1765–1772, <https://doi.org/10.1021/cs3003098>.
- [9] I. Roger, M.A. Shipman, M.D. Symes, Earth-abundant catalysts for electrochemical and photoelectrochemical water splitting, *Nat. Rev. Chem.* 1 (2017) 0003, <https://doi.org/10.1038/s41570-016-0003>.
- [10] J. Yan, Z. Yao, J. Mieteck, Q.S. Zhang, Design of electrocatalysts for oxygen- and hydrogen-involving energy conversion reactions, *Chem. Soc. Rev.* 44 (2015) 2060–2086, <https://doi.org/10.1039/c4cs00470a>.
- [11] W. Zhou, X.F. Lu, J.J. Chen, T. Zhou, P.Q. Liao, M. Wu, G.R. Li, Hierarchical porous prism arrays composed of hybrid Ni/NiO carbon as highly efficient electrocatalysts for overall water splitting, *ACS Appl. Mater. Interfaces* 10 (2018) 38906–38914, <https://doi.org/10.1021/acsami.8b13542>.
- [12] L. Zhao, W. Niu, Z. Le, Y. Yang, Phosphorus and aluminum Co doped porous NiO nanosheets as highly efficient electrocatalysts for overall water splitting, *ACS Energy Lett.* 3 (2018) 1562–1563, <https://doi.org/10.1021/acsenergylett.8b00901>.
- [13] Z. Shen, X. Yu, Y. Feng, C. Li, X. Zhang, Y.J. Chen, N-doped graphene-supported Co@CoO core-shell nanoparticles as high-performance bifunctional electrocatalysts for overall water splitting, *J. Mater. Chem. A* 4 (2016) 12046–12053, <https://doi.org/10.1039/c6ta04365h>.
- [14] L.L. Feng, G.T. Yu, Y.Y. Wu, G.D. Li, H. Li, Y.H. Sun, T. Asefa, W. Chen, X.X. Zou, High-index faceted Ni₃S₂ nanosheet arrays as highly active and ultrastable electrocatalysts for water splitting, *J. Am. Chem. Soc.* 137 (2015) 14023–14026, <https://doi.org/10.1021/jacs.5b08186>.
- [15] J.J. Lv, J. Zhao, H. Fang, L.P. Jiang, L.L. Li, J. Ma, J.J. Zhu, Incorporating nitrogen-doped graphene quantum dots and Ni₃S₂ nanosheets: a synergistic electrocatalyst with highly enhanced activity for overall water splitting, *Small* 13 (2017) 1700264, <https://doi.org/10.1002/sml.201700264>.
- [16] C.Z. Yuan, Z.T. Sun, Y.F. Jiang, Z.K. Yang, N. Jiang, Z.W. Zhao, U.Y. Qazi, W.H. Zhang, A.W. Xu, One-step in situ growth of iron-nickel sulfide nanosheets on FeNi alloy foils: high-performance and self-supported electrodes for water oxidation, *Small* 13 (2017) 1604161, <https://doi.org/10.1002/sml.201604161>.
- [17] S. Jing, L. Zhang, L. Luo, J. Lu, S. Yin, P. Shen, P. Tsiakaras, N-Doped porous molybdenum carbide nanobelts as efficient catalysts for hydrogen evolution reaction, *Appl. Catal. B: Environ.* 224 (2018) 533–540, <https://doi.org/10.1016/j.apcatb.2017.10.025>.
- [18] Z. Cheng, Q. Fu, Q. Han, Y. Xiao, Y. Liang, Y. Zhao, L. Qu, A type of 1 nm molybdenum carbide confined within carbon nanomesh as highly efficient bifunctional electrocatalyst, *Adv. Funct. Mater.* 28 (2018) 1705967, <https://doi.org/10.1002/adfm.201705967>.
- [19] L. Cao, N. Zhang, L. Feng, J. Huang, Y. Feng, W. Li, D. Yang, Q. Liu, Well-dispersed ultrasmall VC nanoparticles embedded in N doped carbon nanotube as highly efficient electrocatalysts for hydrogen evolution reaction, *Nanoscale* 10 (2018) 14272–14279, <https://doi.org/10.1039/C8NR03930E>.
- [20] L. Zhou, M. Shao, J. Li, S. Jiang, M. Wei, X. Duan, Two-dimensional ultrathin arrays of CoP: electronic modulation toward high performance overall water splitting, *Nano Energy* 41 (2017) 583–590, <https://doi.org/10.1016/j.nanoen.2017.10.009>.
- [21] X. Liang, B. Zheng, L. Chen, J. Zhang, Z. Zhuang, B.H. Chen, MOF-derived formation of Ni₂P-CoP bimetallic phosphides with strong interfacial effect towards electrocatalytic water splitting, *ACS Appl. Mater. Interfaces* 9 (2017) 23222–23229, <https://doi.org/10.1021/acsami.7b06152>.
- [22] P. Wang, Z. Pu, Y. Li, L. Wu, Z. Tu, M. Jiang, Z. Kou, I.S. Amiinu, S. Mu, Iron-doped nickel phosphide nanosheet arrays: an efficient bifunctional electrocatalyst for water splitting, *ACS Appl. Mater. Interfaces* 9 (2017) 26001–26007, <https://doi.org/10.1021/acsami.7b06305>.
- [23] J.M. Falkowski, N.M. Concannon, B. Yan, Y. Surendranath, Heazlewoodite, Ni₃S₂: a potent catalyst for oxygen reduction to water under benign conditions, *J. Am. Chem. Soc.* 137 (2015) 7978–7981, <https://doi.org/10.1021/jacs.5b03426>.
- [24] N. Jiang, Q. Tang, M. Sheng, B. You, D.E. Jiang, Y. Sun, Nickel sulfides for electrocatalytic hydrogen evolution under alkaline conditions: a case study of crystalline NiS, NiS₂, and Ni₃S₂ nanoparticles, *Catal. Sci. Technol.* 6 (2016) 1077–1084, <https://doi.org/10.1039/C5CY01111F>.
- [25] J. Dong, F.Q. Zhang, Y. Yang, Y.B. Zhang, H. He, X. Huang, X. Fan, X.M. Zhang, (003)-Facet-exposed Ni₃S₂ nanoporous thin films on nickel foil for efficient water splitting, *Appl. Catal. B: Environ.* 243 (2018) 693–702, <https://doi.org/10.1016/j.apcatb.2018.11.003>.
- [26] T.A. Ho, C. Bae, H. Nam, E. Kim, S.Y. Lee, J.H. Park, H. Shin, Metallic Ni₃S₂ film grown by atomic layer deposition as an efficient and stable electrocatalyst for overall water splitting, *ACS Appl. Mater. Interfaces* 10 (2018) 12807–12815, <https://doi.org/10.1021/acsami.8b00813>.
- [27] T. Zhu, L. Zhu, J. Wang, G.W. Ho, In-situ chemical etching of tunable 3D Ni₃S₂ superstructures for bifunctional electrocatalysts for overall water splitting, *J. Mater. Chem. A* 4 (2016) 13916–13922, <https://doi.org/10.1039/C6TA05618K>.
- [28] C.S. Rout, B.H. Kim, X. Xu, J. Yang, H.Y. Jeong, D. Odkhuu, N. Park, J. Cho, H.S. Shin, Synthesis and characterization of patronite form of vanadium sulfide on graphitic layer, *J. Am. Chem. Soc.* 135 (2013) 8720–8725, <https://doi.org/10.1021/ja403232d>.
- [29] S. Wang, G. Feng, S. Yang, J. Liao, X. Sun, Graphene oxide-template controlled cuboid-shaped high-capacity VS₄ nanoparticles as anode for sodium-ion batteries, *Adv. Funct. Mater.* 28 (2018) 1801806, <https://doi.org/10.1002/adfm.201801806>.
- [30] G. Yang, B. Zhang, J. Feng, H. Wang, M. Ma, K. Huang, J. Liu, S. Madhavi, Z.X. Shen, Y. Huang, High crystallinity urchin-like VS₄ anode for high-performance lithium ion storage, *ACS Appl. Mater. Interfaces* 10 (2018) 14727–14734, <https://doi.org/10.1021/acsami.8b01876>.
- [31] X.M. Zhang, M.L. Tong, H.K. Lee, X.M. Chen, The first noncluster vanadium(IV) coordination polymers: solvothermal syntheses, crystal structure, and ion exchange, *J. Solid State Chem.* 160 (2001) 118–122, <https://doi.org/10.1006/jssc.2001.9202>.
- [32] K.J.H. Lim, G. Yilmaz, Y.F. Lim, G.W. Ho, Multi-compositional hierarchical nanostructured Ni₃S₂@MoS₂/NiO electrode for enhanced electrocatalytic hydrogen generation and energy storage, *J. Mater. Chem. A* 6 (2018) 20491–20499, <https://doi.org/10.1039/c8ta06023a>.
- [33] M. Gong, W. Zhou, M.C. Tsai, J. Zhou, M. Guan, M.C. Lin, B. Zhang, Y. Hu, D.Y. Wang, J. Yang, Nanoscale nickel oxide/nickel heterostructures for active hydrogen evolution electrocatalysis, *Nat. Commun.* 5 (2014) 4695, <https://doi.org/10.1038/ncomms5695>.
- [34] J. Zhang, T. Wang, D. Pohl, B. Rellinghaus, R. Dong, S. Liu, X. Zhuang, X. Feng, Interface engineering of MoS₂/Ni₃S₂ heterostructures for highly enhanced electrochemical overall-water-splitting activity, *Angew. Chem., Int. Ed.* 128 (2016) 6814–6819, <https://doi.org/10.1002/anie.201602237>.
- [35] M.N. Kozlova, E.D. Grayfer, P.A. Poltarak, S.B. Artemkina, A.G. Cherkov, L.S. Kibis, A.I. Boronin, V.E. Fedorov, Oxidizing properties of the polysulfide surfaces of patronite VS₄ and NbS₃ induced by (S₂)²⁻ groups: unusual formation of Ag₂S nanoparticles, *Adv. Mater. Interfaces* 4 (2017) 1700999, <https://doi.org/10.1002/admi.201700999>.
- [36] W. Chao, T. Wang, J. Liu, Z. Yue, D. Yu, J.K. Cheng, H. Fei, Q. Li, J. Chen, Y. Huang, Facile synthesis of silk-cocoon S-rich cobalt polysulfide as an efficient catalyst for hydrogen evolution reaction, *Energy Environ. Sci.* 11 (2018) 2467–2475, <https://doi.org/10.1039/C8EE00948A>.
- [37] Y. Guo, X. Zhang, X. Zhang, T. You, Defect- and S-rich ultrathin MoS₂ nanosheets embedded in N doped carbon nanofibers for efficient hydrogen evolution, *J. Mater. Chem. A* 3 (2015) 15927–15934, <https://doi.org/10.1039/C5TA03766B>.
- [38] Y. Gong, Z. Xu, H. Pan, L. Yu, Z. Yang, J. Wang, A 3D well-matched electrode pair of Ni-Co-S/Ni-Co-P nanoarrays grown on nickel foam as a high-performance electrocatalyst for water splitting, *J. Mater. Chem. A* 6 (2018) 12506–12514, <https://doi.org/10.1039/C8TA03163K>.
- [39] L. Zeng, K. Sun, Z. Yang, S. Xie, Y. Chen, Z. Liu, Y. Liu, J. Zhao, Y. Liu, C. Liu, Tunable 3D hierarchical Ni₃S₂ superstructures as efficient and stable bifunctional electrocatalysts for both H₂ and O₂ generation, *J. Mater. Chem. A* 6 (2018) 4485–4493, <https://doi.org/10.1039/c7ta10790k>.
- [40] H. Huang, Y. Chang, C. Zhao, X. Han, J. Yang, Z. Liu, S. Li, M. Zhang, J. Qiu, Iron-tuned super nickel phosphide microstructures with high activity for electrochemical overall water splitting, *Nano Energy* 34 (2017) 472–480, <https://doi.org/10.1016/j.nanoen.2017.03.016>.
- [41] I.H. Kwak, H.S. Im, D.M. Jang, Y.W. Kim, K. Park, Y.R. Lim, E.H. Cha, J. Park, CoSe₂ and NiSe₂ nanocrystals as superior bifunctional catalysts for electrochemical and photoelectrochemical water splitting, *ACS Appl. Mater. Interfaces* 8 (2016) 5327–5334, <https://doi.org/10.1021/acsami.5b12093>.
- [42] Y. Gong, Z. Xu, H. Pan, Y. Lin, Z. Yang, X. Du, Hierarchical Ni₃S₂ nanosheets coated on Co₃O₄ nanoneedles arrays on 3D nickel foam as efficient electrocatalyst for oxygen evolution reaction, *J. Mater. Chem. A* 6 (2018) 5098–5106, <https://doi.org/10.1039/c7ta11104e>.
- [43] Y. Yang, K. Zhang, H. Lin, X. Li, H.C. Chan, L. Yang, Q. Gao, MoS₂-Ni₃S₂ hetero-nanorods as efficient and stable bifunctional electrocatalysts for overall water splitting, *ACS Catal.* 7 (2017) 2357–2366, <https://doi.org/10.1021/acscatal.6b03192>.
- [44] A.Y. Lu, X. Yang, C.C. Tseng, S. Min, S.H. Lin, C.L. Hsu, H. Li, H. Idriss, J.L. Kuo, K.W. Huang, High-sulfur-vacancy amorphous molybdenum sulfide as a high current electrocatalyst in hydrogen evolution, *Small* 12 (2016) 5530–5537, <https://doi.org/10.1002/sml.201602107>.
- [45] H. Qin, Z. Yang, L. Chen, X. Chen, L. Wang, A high-rate aqueous rechargeable zinc ion battery based on the VS₄@rGO nanocomposite, *J. Mater. Chem. A* 6 (2018) 23757–23765, <https://doi.org/10.1039/c8ta08133f>.
- [46] G. Silversmit, D. Depla, H. Poelman, G.B. Marin, R.D. Gryse, Determination of the V_{2p} XPS binding energies for different vanadium oxidation states (V⁵⁺ to V⁰⁺), *J. Electron. Spectrosc. Relat. Phenom.* 135 (2004) 167–175, <https://doi.org/10.1016/j.jelspec.2004.03.004>.
- [47] Z.H. Deng, L. Li, W. Ding, K. Xiong, Z.D. Wei, Synthesized ultrathin MoS₂ nanosheets perpendicular to graphene for catalysis of hydrogen evolution reaction, *Chem. Commun.* 51 (2015) 1893–1896, <https://doi.org/10.1039/c4cc08491h>.
- [48] W.W. Guo, D.F. Wu, Facile synthesis of VS₄/graphene nanocomposites and their visible-light-driven photocatalytic water splitting activities, *Int. J. Hydrogen Energy* 39 (2014) 16832–16840, <https://doi.org/10.1016/j.ijhydene.2014.08.088>.
- [49] W. Li, J. Huang, L. Feng, L. Cao, S. He, 3D Self-assembled VS₄ microspheres with high pseudocapacitance as highly efficient anodes for Na-ion batteries, *Nanoscale* 10 (2018) 21671–21680, <https://doi.org/10.1039/c8nr06458j>.
- [50] X.G. Wang, W. Li, D.H. Xiong, L.F. Liu, Fast fabrication of self-supported porous nickel phosphide foam for efficient, durable oxygen evolution and overall water splitting, *J. Mater. Chem. A* 4 (2016) 5639–5646, <https://doi.org/10.1039/c5ta10317g>.
- [51] J.Y. Chen, L. Dang, H. Liang, W. Bi, J.B. Gerken, S. Jin, E.E. Alp, S.S. Stahl, Operando analysis of NiFe and Fe oxyhydroxide electrocatalysts for water oxidation: detection of Fe⁴⁺ by Mössbauer spectroscopy, *J. Am. Chem. Soc.* 137 (2015) 15090, <https://doi.org/10.1021/jacs.5b10699>.
- [52] G. Zhang, Y.S. Feng, W.T. Lu, D. He, C.Y. Wang, Y.K. Li, X.Y. Wang, F.F. Cao, Enhanced catalysis of electrochemical overall water splitting in alkaline media by Fe doping in Ni₃S₂ nanosheet arrays, *ACS Catal.* 8 (2018) 5431, <https://doi.org/10.1021/acscatal.8b00413>.
- [53] W. Xu, F. Lyu, Y. Bai, A. Gao, F. Ji, Z. Cai, Y. Yin, Porous cobalt oxide nanoplates enriched with oxygen vacancies for oxygen evolution reaction, *Nano Energy* 43 (2017) 110–116, <https://doi.org/10.1016/j.nanoen.2017.11.022>.
- [54] M. Asnavandi, Y. Yin, Y. Li, C. Sun, C. Zhao, Promoting oxygen evolution reactions

- through introducing oxygen vacancies to benchmark NiFe-OOH catalysts, ACS Energy Lett. 3 (2018) 1515–1520, <https://doi.org/10.1021/acseenergylett.8b00696>.
- [55] T. Kou, T. Smart, B. Yao, I. Chen, D. Thota, Y. Ping, Y. Li, Theoretical and experimental insight into the effect of nitrogen doping on hydrogen evolution activity of Ni₃S₂ in alkaline medium, Adv. Energy Mater. 4 (2018) 1703538, , <https://doi.org/10.1002/aenm.201703538>.
- [56] Q. Xu, H. Jiang, H. Zhang, Y. Hu, C. Li, Heterogeneous interface engineered atomic configuration on ultrathin Ni(OH)₂/Ni₃S₂ nanoforests for efficient water splitting, Appl. Catal. B: Environ. 242 (2019) 60–66, <https://doi.org/10.1016/j.apcatb.2018.09.064>.